ISSN 1330–0016
CODEN FIZBE7

THE EXPERIMENTAL CHALLENGE OF VIRTUAL COMPTON SCATTERING ABOVE 8 GeV

P. Y. BERTIN[a], Y. ROBLIN[a] and C. E. HYDE-WRIGHT[b]

[a] *Université Blaise Pascal/IN2P3, Clermont-Ferrand, France*

[b] *Old Dominion University, Norfolk VA, U.S.A.*

Received 17 March 1999; Accepted 14 June 1999

We discuss the experimental issues confronting measurements of the virtual-Compton-scattering (VCS) reaction ep→epγ with electron beams of energy 6 − 30 GeV. We specifically address the kinematics of deeply-virtual-Compton-scattering (deep inelastic scattering, with coincident detection of the exclusive real photon nearly parallel to the virtual photon direction) and large transverse momentum VCS (high energy VCS of arbitrary Q^2, and the recoil proton emitted with high-momentum transverse to the virtual photon direction). We discuss the experimental equipment necessary for these measurements. For the deeply virtual Compton scattering, we emphasize the importance of the Bethe-Heitler – Compton interference terms that can be measured with the electron-positron (beam charge) asymmetry, and the electron beam helicity asymmetry.

PACS numbers: 13.60.Fz UDC 539.126

Keywords: deeply virtual Compton scattering, Bethe-Heitler – Compton interference terms, electron-positron (beam charge) asymmetry, electron-beam helicity asymmetry

1. Introduction

Exclusive reactions are a very powerful tool to study the transition between weakly interacting quarks at small distances and large distance effects such as the quark confinement responsible for the hadron structure. One of the cleanest ways to tackle this problem is via virtual Compton scattering (VCS), even though this reaction is experimentally challenging for a number of reasons. First, the cross-section is small and decreases as Q^2 or s increases. Furthermore, the VCS process (ep $\rightarrow$ epγ) has to be separated from a number of concurrent background processes, often with counting rates several times higher than the VCS itself. Until recently, this kind of experiment was not achievable because it requires high beam current, high duty cycle and low emittance. The advent of CEBAF enabled us to perform the first VCS experiment above the pion threshold at high Q^2 and s. This experiment is currently under analysis [1]. In the upcoming years, this machine will be upgraded to 8 GeV, then 12 GeV and perhaps 24 GeV in the future. In the same time, the ELFE project in Europe is planning to use the existing LEP cavities to build a 30 GeV machine with similar beam characteristics (high current, high duty cycle and good energy resolution).

In a contribution to the workshop CEBAF at 8 GeV [3], we stressed the benefits of the VCS approach. This paper will focus on the experimental challenges for VCS experiments above 8 GeV. Our interest in VCS is twofold:

- Deeply virtual Compton scattering (DVCS) corresponding to the diffraction of a virtual photon in the forward direction. DVCS [4–6] allows to access the off forward parton distribution (OFPD) directly linked to the non-perturbative part of the nucleon. The kinematic domain of DVCS is deep inelastic electron scattering (large s and Q^2) with the final photon produced very nearly in the virtual photon direction. For incident energies of 6 to 12 GeV, the accessible domain is in the quark valence regime ($x_{\rm Bj} \approx 0.3$).
- The large P_T domain. This is the domain where s is large and the angle between the real and virtual photons is large (neither near 0 nor near π). Q^2 is moderate or even quasi-real. This probes the quark wave function [6,7].

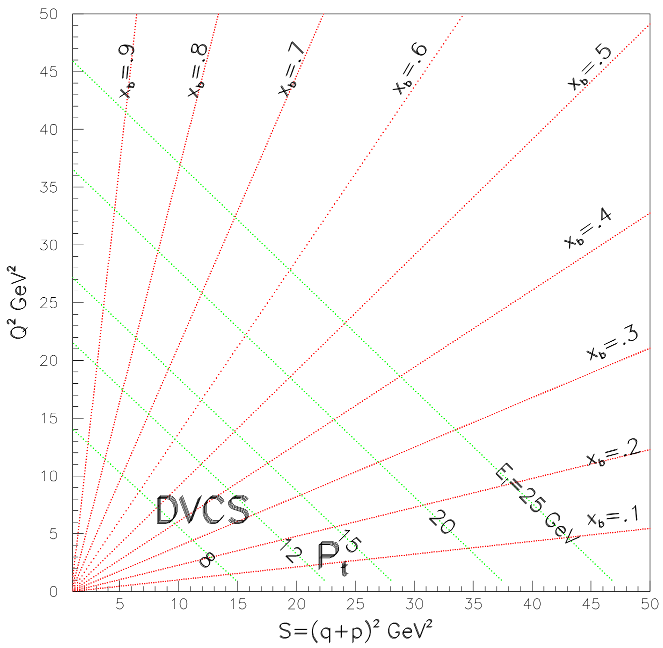

Fig. 1. Ranges in Q^2 and s accessible with an accelerator of incident energy E_i.

Figure 1 shows the kinematic domains relevant for DVCS and large P_T. It also shows the limit on Q^2 and s given an accelerator energy.

2. *Electro-production of a photon*

To the lowest order in α, the three graphs in the top panel of Fig. 2 contribute to the electro-production of a photon. Graph (a) is the VCS and graphs (b) and (c) are the Bethe-Heitler (BH) graphs. The latter two are fully calculable if we know the form factors of the proton, and their amplitude is purely real.

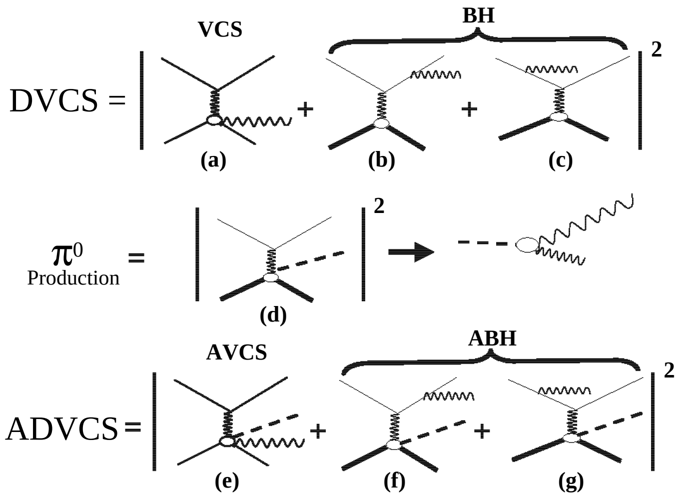

Fig. 2. Lowest-order diagrams of electro-production of photon, pion, or photon plus pion. Top: VCS and BH amplitudes. Middle: π^0 electro-production, which contributes a background ep $\to$ ep$\gamma\gamma$. *Bottom, associated production:* ep$\to$ eγN* (N* $\to$ Nπ).

Due to the propagator of the virtual electron and the virtual photon, three different poles have to be considered in the BH graphs:

$$A^{\rm BH} \sim \frac{1}{t}\frac{1}{(k-q')^2 - m_e^2} + \frac{1}{t}\frac{1}{(k'+q')^2 - m_e^2}\,.$$

These poles determine the shape of the BH cross section at high energy. Since the signs of the electron propagators are opposite in the two BH graphs, there is a strong destructive interference at the $t = (q - q')^2$ pole.

In Fig. 3, BH, DVCS, and large P_T VCS cross sections are evaluated for a particular electron kinematics. The DVCS contribution is evaluated with a model given by P. A. M. Guichon and M. Vanderhaeghen [6]. The OFPD are modeled as the product of the distribution functions and the elastic form factors. The cross section for the large P_T domain is modeled with the virtual photon flux and a scaling ansatz for the photo-production cross section:

$$2\pi \frac{\mathrm{d}^5\sigma}{\mathrm{d}p_e \mathrm{d}\Omega_e \mathrm{d}t \mathrm{d}\phi_\gamma} = \frac{\mathrm{d}\Gamma}{\mathrm{d}p_e \mathrm{d}\Omega_e} s^{-6} (30\ \mu\mathrm{b} \cdot \mathrm{GeV}^{10}).$$

We will use these two models to estimate the counting rates.

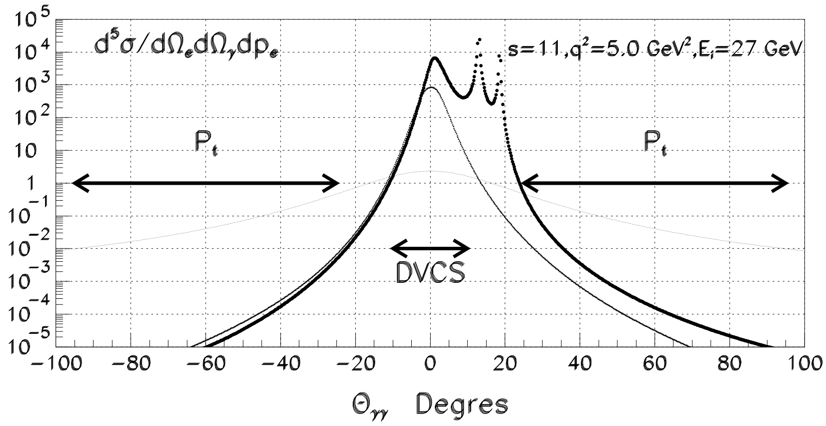

Fig. 3. Cross sections for the ep→epγ *process. Heavy dotted line: Bethe-Heitler; medium line, DVCS; thin line, model for hard scattering (large P_T) VCS. The cross sections are plotted as a function of $\theta_{\gamma\gamma}$, the laboratory opening angle between the virtual photon and emitted real photon directions.*

One of the main difficulties of VCS experiments is to measure a cross-section over several (5 to 8) orders of magnitude. The BH contribution is dominant at the two electron poles. At the photon pole $\theta_{\gamma\gamma} = 0$ ($t = t_{\mathrm{min}}$) BH is also larger than VCS. Far away from these poles, BH becomes much smaller than VCS, and the cross section is small (≈ 1 pb GeV^{-1} sr^{-2}).

The DVCS cross-section by itself is very small and BH makes up most of the total cross-section in the DVCS regime. Fortunately, it is possible to extract DVCS using asymmetries to access the interference term between the DVCS and BH amplitude. This interference has an important contribution to the cross-section, since the BH amplitude is large. This enhancement of DVCS with BH is the key to the measurement of DVCS. There are two kinds of asymmetries that we can use:

- the lepton charge asymmetry, and
- the beam polarization asymmetry.

2.1. Lepton charge asymmetry

This asymmetry is measured by the difference in the cross sections for a negative or positive incident lepton (electron to positron):

- The VCS amplitude, $T_{\rm VCS}$, (diagram (a), Fig. 2) is anti-symmetrical under a charge conjugation, there is only one coupling on the lepton line.
- The BH amplitude, $T_{\rm BH}$, (diagrams (b) and (c), Fig. 2) is symmetrical, there are two couplings onto the lepton line.

Therefore, the interference term between BH and VCS in the cross section is the only term contributing to an electron-positron asymmetry [6]

$$d^5\sigma^{e^-} - d^5\sigma^{e^+} \simeq 4\Re\left[T_{\rm VCS}\cdot T_{\rm BH}\right].$$

This asymmetry is a direct measure of the VCS amplitude since the BH amplitude is fully calculable. We use in the following the asymmetry:

$$A^{e^+/e^-} = \frac{{\rm d}^5\sigma^{e^-} - {\rm d}^5\sigma^{e^+}}{{\rm d}^5\sigma^{e^-} + {\rm d}^5\sigma^{e^+}}.$$

In Fig. 4, we give the value of this asymmetry for three angles $\theta_{\gamma\gamma}$ between the virtual photon and the real photon. It is plotted against the azimuthal angle ϕ between the leptonic and the hadronic plane. This figure is for an incident beam energy of 8 GeV, $s = 8$ GeV^2 and $Q^2 = 3$ GeV^2. From the figure, we see that the asymmetry is large for small angles of the real photon relative to the virtual photon direction.

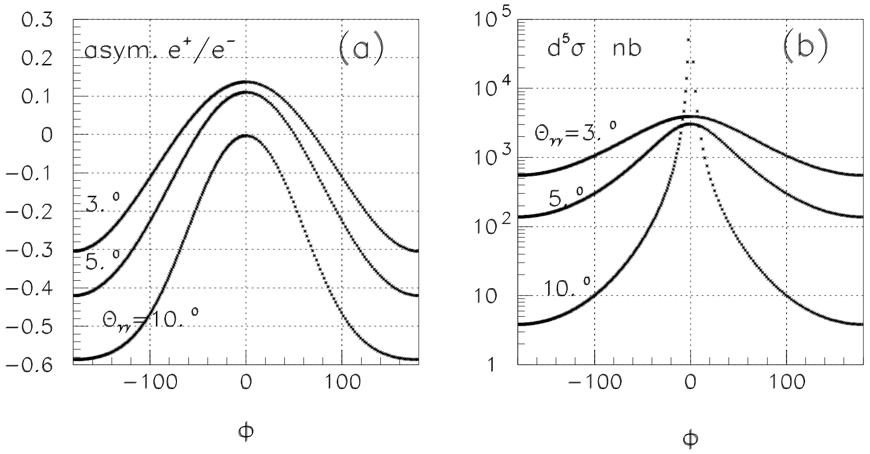

Fig. 4. (a) Asymmetry versus azimuthal angle ϕ induced when the sign of the beam is changed (electron/positron beam). The plot is given at three angles $\theta_{\gamma\gamma} = 3°$, $5°$ and $10°$. (b) The cross section ${\rm d}\,\sigma/({\rm d}\,k_e{\rm d}\Omega_e{\rm d}\Omega^{\rm lab}_{\gamma\gamma})$ in nb/(GeV sr^2) at the same angle. For $\phi = 0$, the emitted photon lies in the scattering plane, closer to the beam than the virtual photon direction. The curves were calculated with the model of Ref. 6. We have chosen the kinematics at $s = 8$ GeV^2, Q^2=3 GeV^{2}and an incident energy $E_i = 8$ GeV.

We think it is very interesting to use this characteristic and that is why we propose to build at CEBAF and at ELFE a positron beam. We will come back to this point later.

2.2. The beam polarization asymmetry.

Another interesting observable is the beam helicity asymmetry

$$A^{\mathrm{Beam}} = \frac{\mathrm{d}^5\sigma^{\rightarrow} - \mathrm{d}^5\sigma^{\leftarrow}}{\mathrm{d}^5\sigma^{\rightarrow} + \mathrm{d}^5\sigma^{\leftarrow}}\,,$$

produced with a polarized beam. This asymmetry is defined as the ratio between the difference and the sum of the cross-sections obtained when reversing the beam longitudinal polarization. Here also, the interference between the BH and the VCS amplitudes is the only term contributing (assuming the longitudinal VCS amplitude is much smaller than the BH one).

This was pointed out in the case of large P_T by Kroll et al. [7,6] and afterwards applied by Diehl et al. [8] and Guichon and Vanderhaeghen [6] in the case of DVCS.

We give in Fig. 5 the value of this asymmetry for the same kinematics as in Fig. 4. The asymmetry deviates slightly from a pure $\sin\phi$ behavior, due to the structure of the BH amplitude. This asymmetry is maximal out of plane ($\phi = \pm 90°$) and is zero when the photon angle $\theta_{\gamma\gamma}$ is zero. Unfortunately, the cross section is maximum when $\theta_{\gamma\gamma}$ is zero. The beam helicity asymmetry will require a larger integrated luminosity to achieve the same precision as the beam charge asymmetry.

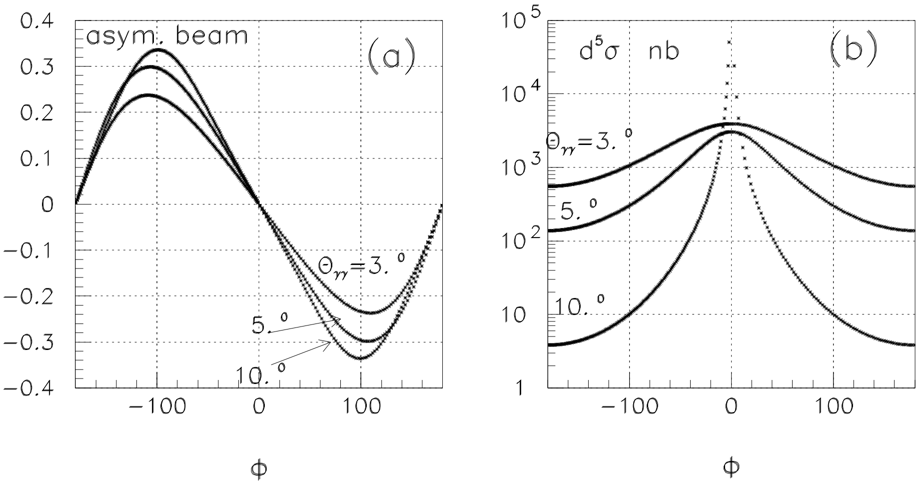

Fig. 5. (a) Asymmetry versus angle induced when the sign of the longitudinal polarization of the beam is reversed. The plot is given at three angles $\theta_{\gamma\gamma}$ 3°, 5° and 10°. (b) The cross section at the same angle. We have chosen the kinematic at $s = 8$ GeV^2, $Q^2 = 3$ GeV^2 *and an incident energy* $E_i = 8$ GeV.

3. *Experimental equipment*

In order to select VCS events (DVCS or large P_T), one must make sure to select photon electro-production events. To do that, we can use the squared missing mass. We need to know:

- the incident particle - that is why it is so crucial to have a good quality beam;
- the scattered electron – it fixes the virtual photon;
- the recoil proton and/or the photon produced. The choice to detect the recoil proton and/or the photon will be fixed by the kinematics and the level of resolution needed.

If the photon is not detected, it is necessary to separate the missing mass zero (photon missing mass) from the pion mass. The squared missing-mass resolution must be

$$\Delta M_X^2 \leq M_\pi^2 \, .$$

If we measure the photon (instead of the proton), the resolution we require on M_X^2 is much looser:

$$\Delta M_X^2 \leq (M_P + M_\pi^2) - M_p^2 \approx 2 M_p M_\pi \, .$$

There is a factor of twenty between the required resolution on the squared missing mass in the two cases.

The best case will be when the photon is detected and measured (momentum and direction) and the proton detected (position only). In that case, we can use not only a missing mass-technique, but also require coplanarity conditions on the virtual photon, the recoil proton and the photon.

3.1. *The Background problem*

There are two main sources of background: the π^0 electro-production, ep→epπ^0 (diagram (d), Fig. 2), and the pion-associated production with photon electro-production, ep→eγN* (diagrams (e), (f) and (g) in Fig. 2).

3.1.1. **The π^0 electro-production.**

The graph of the π^0 electro-production is the (d) graph in Fig. 2. When π^0 decays with a photon emitted in the forward direction, the second photon from the π^0 is backward and has a very low energy (few MeV). The final products of this reaction are nearly the same as a VCS event, except for a soft backward photon which is very difficult to detect at an electromagnetic machine. The missing-mass technique is unable to solve the problem either. The π^0 events are partially removed by a coplanarity cut on triple epγ coincident events. The solution for the remaining π^0 events is to record in the calorimeter events with the π^0 decay at 90° in the centre of mass. The two photons are emitted in the forward direction with comparable energies and their opening angle is $\theta^{\pi}_{\gamma\gamma} \geq 2\, m_{\pi^0}/P_{\pi^0}$. Using these events, we can infer the π^0 cross section and subtract its contribution from the events with only one photon recorded.

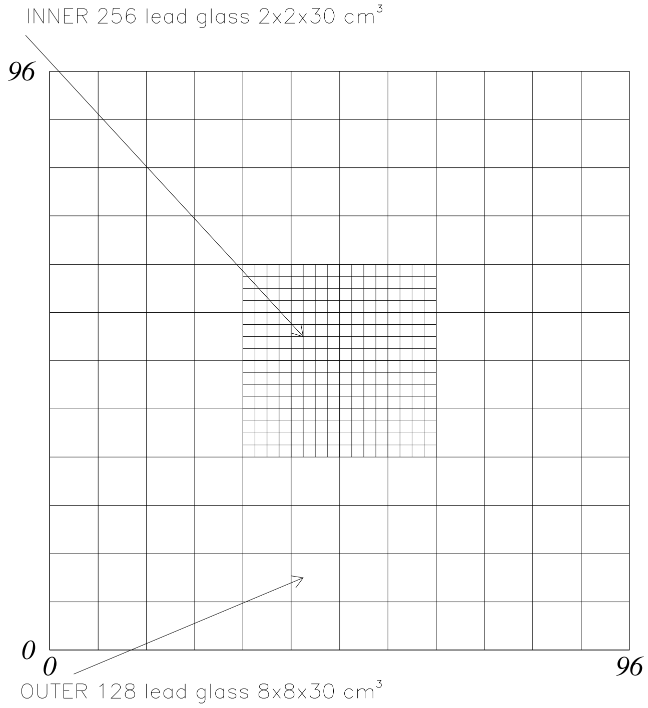

Fig. 6. Calorimeter concept with high inner granularity to record DVCS events and coarser outer granularity to record two-photon events from the ep$\to$epπ^0 *reaction.*

In Fig. 6, we give an example of a composite calorimeter. The inner part, with a small granularity to collect the VCS events, the outer part with a bigger granularity to collect the two-photon events from the π^0 decay.

In the DVCS kinematics, the π^0 production:

- decreases as $1/Q^6$, faster than DVCS which decreases as $1/Q^4$,
- has no interference with BH, contrary to VCS which is amplified by BH when the quadri-transfer t is small, and
- has no beam charge-dependent asymmetry. Thus this background vanishes completely in A^{e^+/e^-}.

We should point out that the π^0 cross section is in itself a very interesting result. In DVCS kinematics, it is sensitive to another combination of the OFPD [9].

3.1.2. **The associated pion production.**

Another parasitic reaction is the associated pion production at the photon electroproduction. The corresponding graphs are Fig. 2 (e), (f) and (g). The last two graphs ((f) and (g)) show the associated pion production with the BH process (ABH). The ABH process can be exactly predicted, given the knowledge of the p→N* transition form factors (instead of the proton form factors as in VCS). The third graph (AVCS) is the pion production in the VCS. It leads to the same final state as shown by the (e) and (f) graphs and, therefore, the three graphs interfere.

The physics of associated production in DVCS (f) is just as important as physics of the DVCS process. For example, for pion-nucleon system at the mass of Δ (or higher N*), ADVCS gives access to some of the N→ N* transition OFPDs. However, it is not so simple to extract the ADVCS amplitude, since in this case ABH is no longer purely real but also has an imaginary part (because of the intermediate on-shell N* state). Close to the pion threshold (πN system in s-wave), a low-energy theorem can be built to relate the p→Nπ OFPDs to the elastic OFPDs.

Under the charge change of the lepton, the associated pion production has an asymmetry similar to the DVCS case.

If the proton is not detected, the associated pion production can appear in either the π^0p or π^+n final states. If the recoil proton is detected, only the π^0 channel is open.

3.2. Positron beam

We have pointed out the interest of the charge asymmetry. But to access this information, we need a positron beam. Several techniques can be used such as radioactive sources, but the main technique is to produce positrons on a heavy material target. This yields positrons of about 60 MeV, which are then collected and injected into the linac. This does not require any significant changes in the linac setup (Fig. 7). Positrons can just be injected into the linac with an RF phase

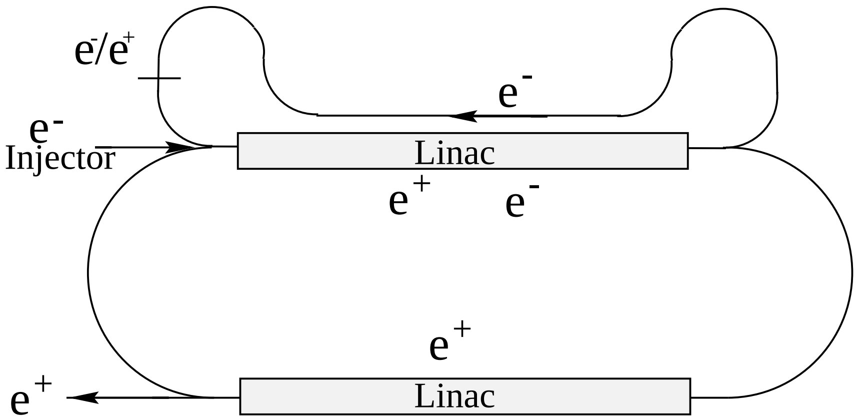

Fig. 7. Possible setup of a positron beam at CEBAF.

difference of 180° relative to the electrons. The positron yield is proportional to the electron beam power on the conversion target. Table 1 [10] lists the parameters of the positron source used at SLC, the parameters of the source for the Next Linear Collider (NLC). The CEBAF extrapolation is obtained by scaling the to the CEBAF beam power on the conversion target [10]. We have given for CEBAF two extrapolations, (a) and (b), based on the SLC number and the NLC Project. The latter gives a larger positron yield due to an improved positron collection. We can conclude that a positron beam is realistic for CEBAF. Because the asymmetry is large, we do not need a rapid switching from electrons to positrons. We need to switch the beam (reverse the polarity of the arc magnets) approximately once every 100 hours.

The following modifications need to be done on the beam line to provide a positron beam:

- a new magnet at the end of the north linac,
- a beam transport line in the north tunnel,
- a room for the positron target and the optics to collect the positrons, and
- a 80 KW beam dump for 0.5 GeV beam.

TABLE 1. Positron production from the SLC-94 and the Next Linac Collider II (NLC-II) [10]. The estimation for CEBAF is obtained by scaling with the CEBAF beam power (a) on SLC, or (b) on the future project NLC-II, which increases the parameter of the positron collection.

Parameters	SLC94	NLC-II	CEBAF
Electron Beam Drive			
Electron Energy (GeV)	30	6.22	0.5
Bunches by pulse	1	75	
Repetition Rate (Hz)	120	120	
Bunch Intensity (e^-)	$3.5 \cdot 10^{10}$	$1.5 \cdot 10^{10}$	
Pulse Intensity (e^-)	$3.5 \cdot 10^{10}$	$113. \cdot 10^{10}$	
Intensity (e^-/ s)	$4.20 \cdot 10^{12}$	$1.35 \cdot 10^{14}$	$1.00 \cdot 10^{15}$
Intensity (μA)	0.67	21.6	160
Beam Power (KW)	20.2	134	80
Positron Collection			
Yield (e^+ per e^-)	2.4	2.1	$\approx$ (a) 0.04 (b) 0.17
Intensity ($10^{14} e^-/s$)	0.108	2.84	(a) 0.4 (b) 4.3
Intensity (μA)	1.7	45.8	$\approx$ (a) 6.4 (b) 27

3.3. Electron spectrometer

When one detects the scattered electron, one must overcome two difficulties:

- reach small angles to do the physics of interest, and
- have large enough solid angle to insure high counting rate.

This must be done keeping a high momentum acceptance ($\Delta P/P = 5 - 10\%$) and a momentum resolution of 10^{-4}.

It is not difficult to go to small angles, but this is often at the expense of the solid angle. For example, experiment E154 at SLAC reaches $\theta_e = 5.5°$ with a solid angle $\Omega = 0.5$ msr, and $\theta_e = 2.75°$ with $\Omega = 0.15$ msr. Several solutions are possible to boost the solid angle while still using small angles:

- Use of $\cos n\theta$ magnets such as was proposed by Vernin et al. for the ELFE project [11,12] or by Finn et al. [13] for 8 – 12 GeV at CEBAF. This solution gives a good spectrometer acceptance ($\Omega = 6.8$ msr) and $\Delta P/P = 20\%$ in the case of ELFE project at 15 GeV.
- Use the septum magnet. It is currently being build by the INFN group for the CEBAF high resolution spectrometer (HRS). It will be possible to reach 6° with a solid angle of $\Omega = 6$ msr.
- If a smaller angle is desired (smaller than 1°), this can be done using a setup using quadrupoles, like the Møller setup in the Experimental Hall A.

3.4. Photon calorimeter

The specifications of the photon calorimeter are very different if we consider physics at large momentum transfer or DVCS kinematics. The next two sections list the requirements on the apparatus for each type of experiment.

3.4.1. **Large P_T H(e,e'pγ) measurements**

In this case, the main purpose of the calorimeter is to suppress the accidentals in the reaction. It must be used at very high luminosity ($(1-2)\cdot 10^{38}$ cm^{-2}s^{-1}) and will be placed at large angle (50°). It does not need a high energy resolution (30 – 50 %), rather it must have a large acceptance coverage (1.5 sr). This calorimeter can be shielded from the low energy gamma rays and can be close to the target. It can be built in a lead chamber or in a lead/plastic sandwich. The fact that it must be able to remove accidentals requires a moderate granularity. That granularity needs to be somewhat better if it is necessary to identify the π^0 decay. The two decay photons are emitted at an angle of $\theta_{\gamma\gamma} = 2m_{\pi^0}/P_{\pi^0}$. This is roughly two degrees at $s = 20$ GeV^2, $Q^2 = 5$ GeV^2 and an incident energy of 27 GeV. The photon energy at the maximum P_T=2.1 GeV is $q' = 6.6$ GeV. If the granularity is good enough, one can also use it for coplanarity cuts (requiring that the detected photon, the recoil proton and the VCS virtual photon all lie in the same plane)

3.4.2. DVCS

In this case, the calorimeter will be placed in a forward direction ($10° - 20°$) where the electromagnetic background coming from the target is a limiting factor for the luminosity, a few 10^{37} cm^{-2}s^{-1} instead of 10^{38} cm^{-2}s^{-1}. Solid angle of the calorimeter is also much smaller (10 msr) than in the case of large P_T. This is just a fact due the to Jacobian. But if we want solve the missing photon from the π^0 decay, this acceptance must be increased to cover the two-photon decay of the π^0:

$$\Omega^{\pi}_{\gamma\gamma} \gg (\frac{2m_{\pi^0}}{P_{\pi^0}})^2.$$

TABLE 2. Minimum calorimeter acceptance, Ω, required to measure the π^0 electro-production cross section for the subtraction from DVCS. We also give the required separating power $\Delta\Theta$ of two photons in the calorimeter to resolve the two photons in $\pi^0 \to \gamma\gamma$ decay.

s GeV^2	Q^2 GeV^2	E_i GeV	P_γ GeV	Ω msr	$\Delta\Theta$ mr
6	1	6	3.2	7.4	86.
8	3	8	5.3	2.7	52.
11	5	16	8.0	1.3	36.
15	7	27	11.2	0.6	25.

One must stress again that if we work with charge asymmetry, (electron-positron), then the electro-production of π^0 is gone (it does not contribute to the asymmetry) and our only worry is the associated pion production. To distinguish between the associated pion production and the H(e,e'γ)p reaction, we need an energy resolution on the photon:

$$\Delta P_\gamma \ll \frac{M_p m_\pi}{P_X}$$

or we have to detect the recoil proton to check for coplanarity.

In Fig. 8, we give in a plot (Q^2 vs. s) of the required photon resolution for one sigma separation of the p and Nπ final states in the H(e,e'γ)X reaction. In order to estimate the precision of the energy measurement of the photon, we consider three kinds of crystals:

- lead tungstate used in the CMS calorimeter [14] giving a resolution (when the crystal is seen by APD):

$$\frac{\sigma_E}{E} = 0.035 + \frac{0.036}{\sqrt{E}},$$

- F101 radiation-resistant lead glass [15]; the resolution

$$\frac{\sigma_E}{E} = 0.015 + \frac{0.051}{\sqrt{E}}$$

  is obtained with a preshower compensation,

- CsI(Ti) used by BaBar at SLAC [16]; the resolution is

$$\frac{\sigma_E}{E} = 0.012 + \frac{0.01}{\sqrt[4]{E}}.$$

  This calorimeter is without any doubt one of the best on the market. If we want to go to higher energy, we can use a pair spectrometer with a converter and a magnetic field.

From Fig. 8, we can see that at moderate s (smaller than 10 GeV^2), it is possible to build a calorimeter meeting all the specifications for the DVCS.

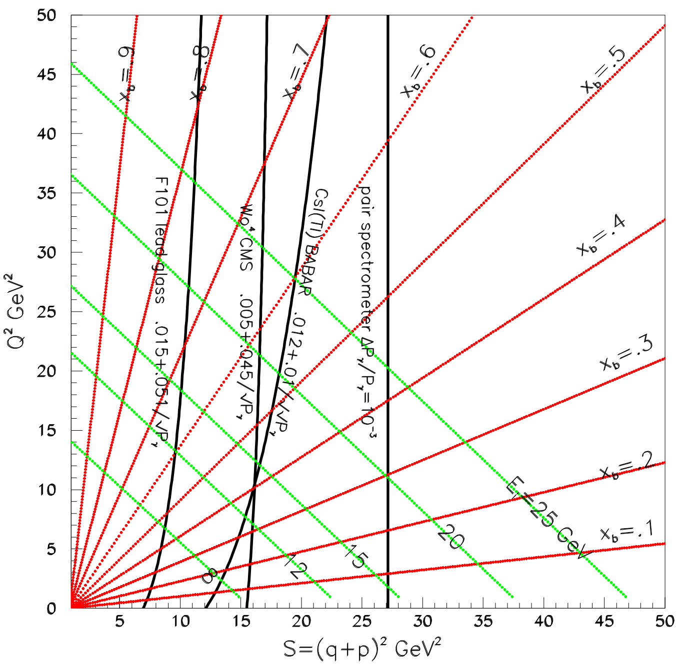

Fig. 8. Photon resolution on a plot Q^2 vs. s.

High luminosity will be the main issue for the calorimeter, mainly for the forward angles where the electromagnetic background coming from the target will be large (Møller, radiative Møller, scattered electrons...). Several tests done in Hall A for the

RCS experiment 97-108 have already shown that working at a luminosity of a few 10^{37} cm^{-2} s^{-1} is possible. In order to deal with the pile-up in the calorimeter, we will use a new technology based on high speed sampling (1 GHz) on the calorimeter channels.

3.5. Proton detector

There are two different approaches for the proton detectors depending on what we want to measure:

- In the case of VCS at large P_T, we use the reconstructed proton momentum to build the missing mass and identify the reaction. This means, one needs a high resolution spectrometer (the same level of performance one has in the electron arm). A design with $\cos n\theta$ magnets is discussed in Refs. 11 and 12].
- In the case of DVCS, we may only need to perform coplanarity tests. It is possible to chose kinematics such that the angle $\theta^{lab}_{P,\gamma^v}$ between the recoil proton and the virtual photon in the laboratory frame is large. The centre-of-mass angle corresponding to this kinematic is small and this is a DVCS kinematics (small t). Figure 9 shows some possible kinematics at several incident energies and Q^2 and s.

  the proton and the virtual photon, in the $\mathrm{H}(e,e'p\gamma)$

TABLE 3. Kinematics of the maximum angle $\theta^{Lab}_{P\gamma^v}$ between the proton and the virtual photon, in the H(e,e'pγ) *reaction.*

s GeV^2	Q^2 GeV^2	E_i GeV	θ_{cm} deg.	$\theta_{p\gamma}$ deg	P_P GeV	$\theta_{\gamma\gamma^v}$ deg.
6	1	6	23.	53.	0.51	7.5
6	2	6	30.	42.	0.77	8.5
8	3	8	27.	42.	0.85	6.5
11	5	16	23.	40.	0.94	4.6
15	7	27	20.	40.	0.98	3.4

Table 3 gives several examples of DVCS kinematics computed at the maximum angle in the lab between the proton and the virtual photon. At this angle, the Jacobian $J = \mathrm{d}\,\Omega^{cm}_P/\mathrm{d}\,\Omega^{lab}_P$ is maximal (meaning our CM solid angle is maximal).

From this table several conclusions can be deduced:

1) The proton momentum is high. In this table, the lowest P_P=0.551 GeV has a range of 20 g cm^{-2} in iron. This implies that we can shield the

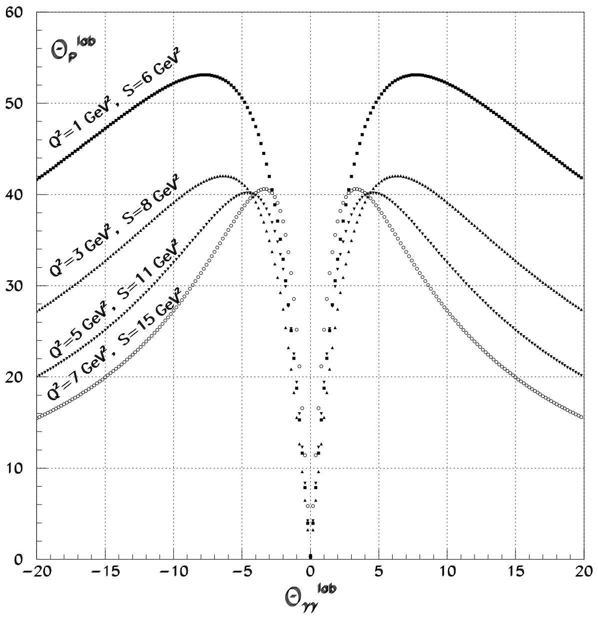

Fig. 9. Recoil proton angle versus emitted photon angle in the laboratory frame for the H(e,e'pγ) *reaction. Both angles are measured relative to the virtual photon direction.*

proton detector from low-energy particles without losing in efficiency on the proton detection. Since most of the high-noise counting rate is at low energy, this also has the benefit to allow the use of high luminosities.

2) The angle between the virtual photon and the real photon is small. Thus, we can place the photon calorimeter in the direction of the virtual photon. This calorimeter can have a small angular acceptance and we will still be able to catch the real photon. The optimum position is a tradeoff between this angle and the electron spectrometer acceptance.

3) The angle between the proton and the virtual photon is large (the smallest in the Table 3 is 40°). The virtual photon is close to the forward direction, ($10° - 20°$), the proton detector, however, will be farther, thus less sensitive to background, allowing to work at high luminosities.

- The solution proposed for the photon calorimeter to solve the pile-up problem based on sampling at 1 Gigahertz will also nicely improve the detection of the proton.

Finally, we can propose the experimental setup sketch presented in Fig. 10. The proton detector is a ring of plastic scintillators located around the direction of the virtual photon. The ring is partially open in the forward direction to let the beam and the scattered electron through.

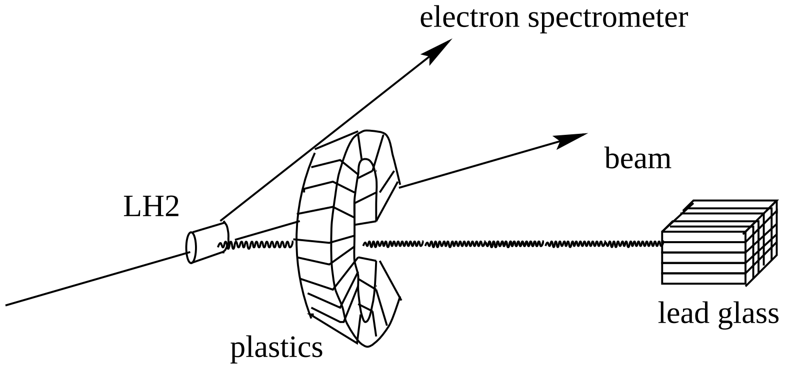

Fig. 10. Proposed experimental setup for DVCS.

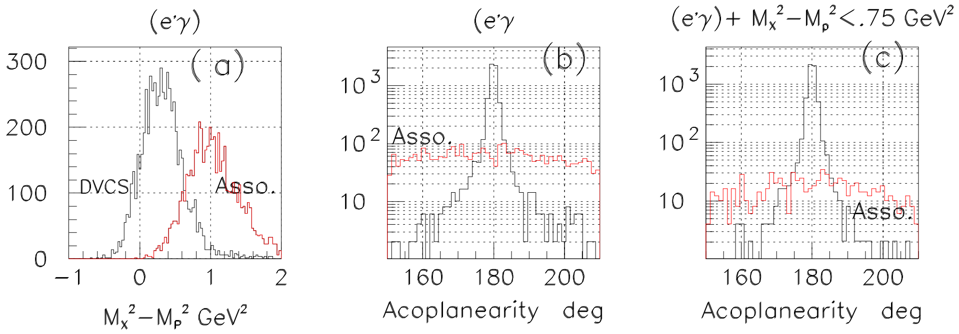

Fig. 11. Missing mass plot and acoplanarity spectra for the ep→epγ *and* ep→eN$\gamma\pi$ *reactions. Kinematics is at* Q^2=3 GeV^2, s = 8 GeV^2, *and 8 GeV incident energy. The electron spectrometer HRS is at 19.9°* *with a solid angle of 6* msr. *The inner photon calorimeter is located at -11.9° and its solid angle is 40* msr. *The density of the events on this plot is just given by the phase space, there is no cross-section weighing. (a) Missing mass squared for* H(e,e'γ)X. *(b) Out of plane angle between final photon and proton for* H(e,e'γp) *and* H(e,e'γp)π^0 *reactions. (c) Same as (b), but with a cut on missing mass spectrum of a).*

In Figs. 11 and 12, the plots (a) show the separation between p(e,e'γ)p and p(e,e'γ)N*, achievable using only the electron and the photon information. The plots (b) and (c) show the discriminatory power of the coplanarity distribution using a proton array to measure p(e,e'γp)X events. The plots (b) and (c) are without and with a cut on the missing mass obtained in (a).

Figures 13 and 14 show the intercept of the recoil protons with the plane defined by the array of scintillators. Plots (a) and (c) show the DVCS events, plots (b) and (d) show the associated production events. Plots (a) and (b) are for all of the corresponding events, plots (c) and (d) are after the cut on missing mass from Figs. 11 and 12 was applied. The protons of the DVCS and the associated events do not have the same distribution. The phase space (4-body) of the associated production events is evenly spread on the acceptance, whereas the DVCS events are concentrated in a ring at the edge of the phase space. This is even more marked if we require a cut on the missing mass obtained with the electron and the photon.

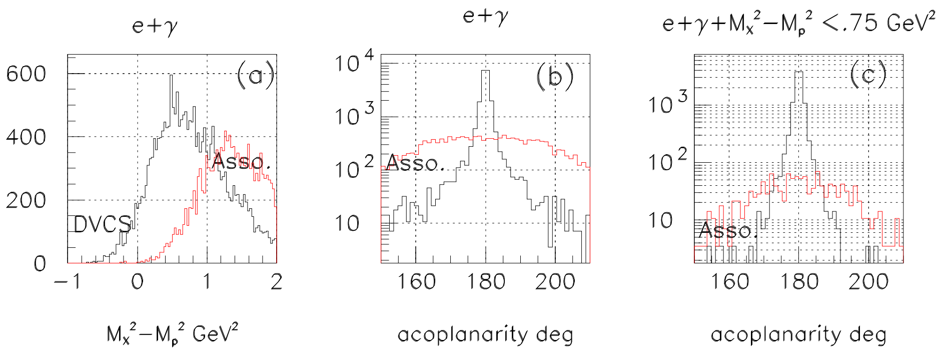

Fig. 12. Missing mass plot and acoplanarity spectrum. Kinematics is at $Q^2 = 5$ GeV^2, $s = 11$ GeV^2, *27* GeV *energy incident. The electron spectrometer is a new spectrometer at 5.7° with a solid angle of 2* msr. *The inner photon calorimeter is located at* $-10.0°$ *and this solid angle is 40* msr. *The density of the events on this plot is just given by the phase space, there is no cross-section weighing. The plots are the same as in Fig. 11.*

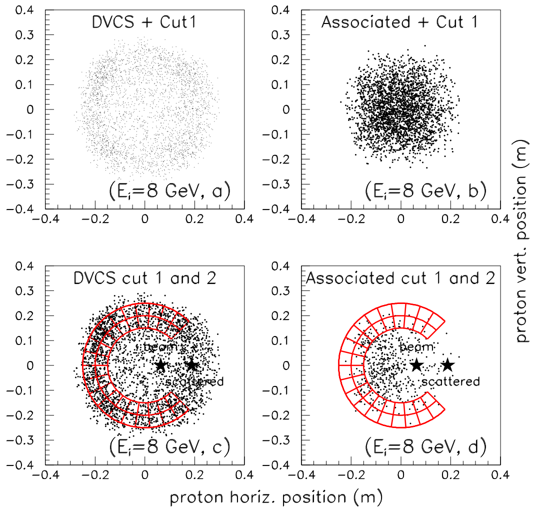

Fig. 13. Localization of the proton in a plane perpendicular to the mean virtual photon direction, 30 cm *from the* LH_2 *target. Kinematics is at* $Q^2 = 3$ GeV^2, $S = 8$ GeV^2, *8* GeV *energy incident. The electron spectrometer HMS is at 19.9° with a solid angle of 8* msr. *The inner photon calorimeter is located at -11.9° and this solid angle is 40* msr. *Note that the density of the events is just given by the phase space. The proposed array of proton detectors is also illustrated.*

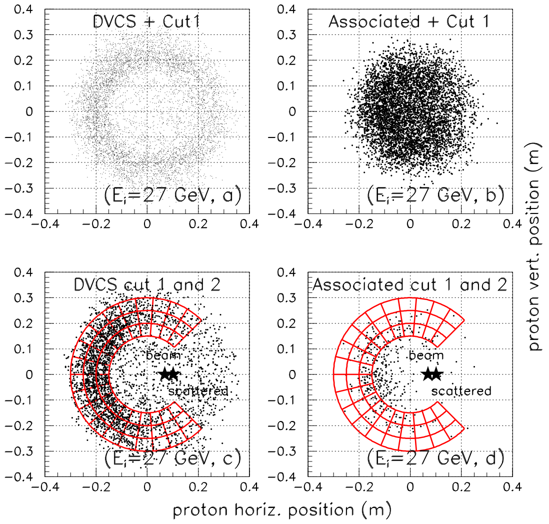

Fig. 14. Localization of the proton in a plane perpendicular to the mean virtual photon direction, 30 cm *from the* LH_2 *target. Kinematics is at* $Q^2 = 5$ GeV^2, $s = 11$ GeV^2, *27* GeV *energy incident. The electron spectrometer is a new spectrometer at 5.7°* *with a solid angle of 2* msr. *The inner photon calorimeter is located at -12.9°* *and this solid angle is 40* msr. *Note that the density of the events is just given by the phase space.*

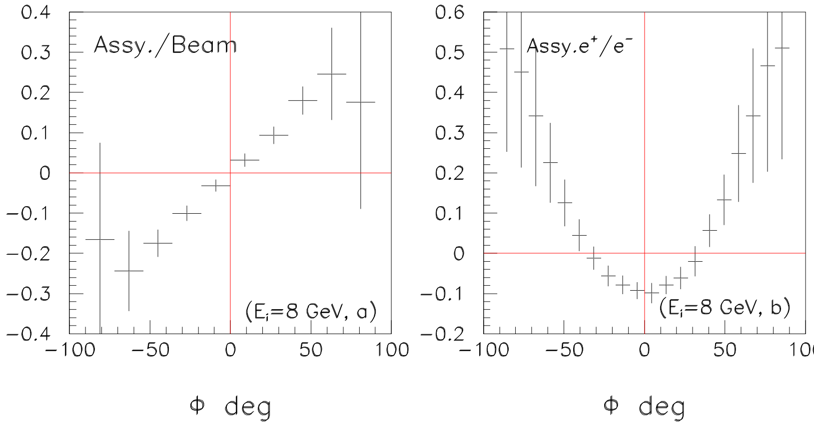

Fig. 15. Expected asymmetry: a) with the polarization of the beam (b) with the beam charge, in a 400 h *of beam time at a luminosity of* 10^{37} cm^{-2}s^{-1}. *Kinematics is at* $Q^2 = 3$ GeV^2, $s = 8$ GeV^2, *8* GeV *energy incident. The electron spectrometer HMS is at 19.9°* *with a solid angle of 8* msr. *The inner photon calorimeter is located at -11.9°* *and this solid angle is 40* msr. *The definition of* ϕ *is the same as in Figs. 4 and 5.*

Figures 15, 16 and 17 give for three kinematics the expected yield for measurements of the beam-charge and beam-helicity asymmetries. This simulation was

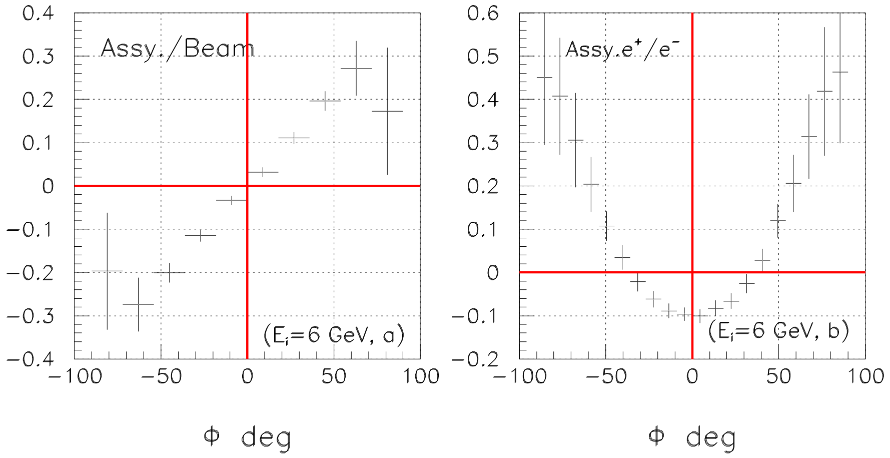

Fig. 16. Expected asymmetry: a) with the polarization of the beam (b) with the beam charge, in 400 h *of beam time at a luminosity of* 10^{37} cm^{-2}s^{-1}. *Kinematics is at* $Q^2 = 2$ GeV^2, $s = 6$ GeV^2, *6* GeV *energy incident. The electron spectrometer HMS is at 22.4° with a solid angle of 8* msr. *The inner photon calorimeter is located at -11.9° and its solid angle is 40* msr.

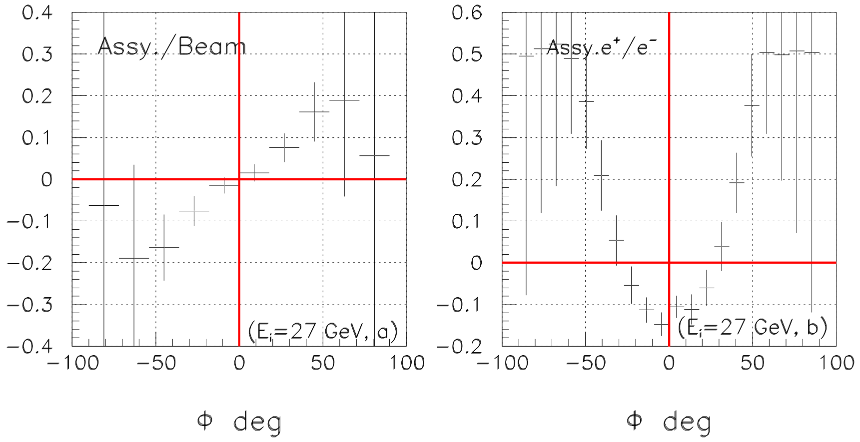

Fig. 17. Expected asymmetry: a) with the polarization of the beam, b) with the beam charge, in 400 h *of beam time at a luminosity of* 10^{37} cm^{-2}s^{-1}. *Kinematics is at* $Q^2 = 5$ GeV^2, $s = 11$ GeV^2, *27* GeV *energy incident. The electron spectrometer is new spectrometer at 5.7° with a solid angle of 2* msr. *The inner photon calorimeter is located at -12.9° and its solid angle is 40* msr.

done using the code "BITCH" [17], which takes into account the resolution of the spectrometer, multiple scattering in the target, and the DVCS cross section model of Ref. 6. It must be noted that in the two lowest-energy settings (6 and 8 GeV), the electron spectrometer corresponds to the CEBAF HRS spectrometer. At 16 and 27 GeV, the angular acceptance is much smaller. The calorimeter is a lead glass calorimeter with a preshower compensation. No attempt was made to optimize the size of this calorimeter for counting rate (at 6 and 8 GeV, the counting rate can be increased by using a bigger calorimeter surface). These asymmetries contain the physics of OFPD. The Q^2 evolution (at fixed x_{Bj}) of these asymmetries is a direct test of the theoretical framework of DVCS, independent of any model of the OFPD [8].

4. *Experimental details for large P_T physics*

In Table 4, we give the counting rate per day for several incident energies and kinematics. Since the large P_T domain can be reached by two symmetrical kinematics around the virtual photon, it is possible to place the proton spectrometer at the same side (relative to the electron beam, positive angles) as the electron spectrometer. The photon calorimeter is then placed in the opposite hemisphere (negative angle). We can chose a centre-of-mass angle not too far from 90° which maximizes P_T. If we want to increase the solid angle (linked to the proton Jacobian $\mathrm{d}\,\Omega^{cm}/\mathrm{d}\,\Omega_p$), we can put the calorimeter in the backward direction. This will also decrease the electromagnetic background, allowing the work at higher luminosities.

We have assumed a low angular acceptance of the electron spectrometer (2.5 msr), compatible with the small angles. Since the proton spectrometer is at larger angle, we have taken the HRS CEBAF spectrometers solid-angle acceptance.

The purpose of the photon calorimeter is only to add a third-arm coincidence to reject accidentals. Therefore, it does not need a high energy resolution. It can be done with a sandwich of lead and plastic scintillators. A lead sheet should be placed in front to protect it from low-energy X-rays and photons. We will then just set a threshold on this calorimeter response to get rid of the low-energy noise.

The photon calorimeter angular range is large, since it has to match the proton acceptance, $\mathrm{d}\Omega_\gamma = \mathrm{d}\Omega_p \times (\mathrm{d}\Omega^{cm}/\mathrm{d}\Omega_p) \times (\mathrm{d}\Omega_\gamma/\mathrm{d}\Omega^{cm})$.

For the large P_T reaction, the associated BH amplitude is small, and will be not enhanced by ABH. This means, it will be smaller than in the DVCS case, so it should not be a problem. On the other hand, the pion electro-production is becoming relevant in this kinematics. We will use the missing-mass cuts to select our events. The missing mass will be constructed with the scattered electron and the recoil proton. If this is not enough, then we can use the photon calorimeter granularity for coplanarity cuts. The acoplanar events will be used to obtain the π^0 cross section. We will then subtract their contribution from the coplanar events to get a clean signal.

The counting rates are given per day. It must be noted that in this example we tried to reach the highest s and the biggest Q^2. However, the cross section and the counting rate decrease as s^{-6}. Going from $s = 15$ GeV^2 to $s = 12$ GeV^2 increases the counting rate by a factor 3.8. Decreasing Q^2 also increases the counting rate.

TABLE 4. Large P_T: Counts obtained in 1 day, with a beam of 80 μA, 10 cm thick liquid hydrogen target, an electron spectrometer of 2.5 mr, a momentum acceptance of ±2.5% and an acceptance of 7 mr for the proton spectrometer. The detection of photon is assumed to match the acceptance of the proton spectrometer.

$\theta_{cm}^{\gamma\gamma}$	P_T	θ_{γ}^{lab}	θ_{p}^{lab}	P_p	$\frac{d^5\sigma}{dP_e\, d\Omega^{cm}}$	$\frac{d\Omega^{cm}}{d\Omega_{\gamma}^{\mathrm{lab}}}$	$\frac{d\Omega^{cm}}{d\Omega_{p}^{\mathrm{lab}}}$	N
deg	GeV	deg	deg	GeV	$\frac{\mathrm{pb}}{\mathrm{GeV\,sr^2}}$			day^{-1}
$E_i = 8$ GeV, $s = 8$ GeV^2, $Q^2 = 0.5$ GeV^2, $\theta_e = 7.22°$, $p_e = 3.9$ GeV								
90	1.25	+27.6	−35.7	2.22	.406	3.12	5.1	120
120	1.08	+49.6	−24.7	3.57	.406	1.07	8.5	200
$E_i = 12$ GeV, $s = 10$ GeV^2, $Q^2 = 1.0$ GeV^2, $\theta_e = 6.43°$, $p_e = 6.6$ GeV								
90	1.44	+22.2	−33.5	3.31	.139	4.0	6.1	82
120	1.24	+42.0	−23.5	4.60	.139	1.28	10.6	149
$E_i = 27$ GeV, $s = 11$ GeV^2, $Q^2 = 5.0$ GeV^2, $\theta_e = 5.7°$, $p_e = 18.9$ GeV								
60	1.32	−25.5	+15.4	2.78	.085	15.7	4.9	149
70	1.43	−28.2	+11.9	3.41	.085	12.8	6.6	160
$E_i = 27$ GeV, $s = 15$ GeV^2, $Q^2 = 2.0$ GeV^2, $\theta_e = 3.6°$, $p_e = 18.4$ GeV								
120	1.58	+32.7	−20.7	7.03	.041	1.78	15.4	175
90	1.82	−31.7	+13.9	4.96	.041	6.05	8.2	96

5. *Conclusion*

We have shown that from 6 to 27 GeV, it is possible to access experimentally VCS, DVCS and VCS at large P_T. For the DVCS, up to $s \leq 15$ GeV^2 and $Q^2 \leq 7$ GeV^2 (for $x_{\mathrm{Bj}} \approx 0.3$). We have shown that for the large P_T VCS ($P_T = 1.9$ GeV), we can reach $s = 15$ GeV^2 and Q^2=2 GeV^2. We have also shown that the apparatus (detector) is feasible. We already did experiments at this level of accuracy (CEBAF), momentum (SLAC) and background (RCS studies at CEBAF). It is also evident that a positron beam would be a big advantage for DVCS. We believe that it is technically possible to have such a beam at CEBAF. It is almost a requirement for the new ELFE machine to be able to deliver both electron and positron beams since so much physics can benefit from it.

Acknowledgements

We thank P. A. M. Guichon, M. Vanderhaeghen, A. V. Radyushkin and M. Diehl for many fruitful discussions, and for their interest in developing this physics. We want to point out especially P. A. M. Guichon who gave us the code we used to evaluate the DVCS and BH processes. P. Y. B. and Y. R. have done this work for the European network (HaPHEEP). The work of C. E. H.-W. was supported by the U. S. Deptartment of Energy and N. S. F.

References

1) G. Audit et al., Jefferson Lab Experiment E93050; http://www.jlab.org/˜ luminita/vcs.html
2) G. Geschonke and E. Keil, CERN SL/98-060(rf);
3) C. Hyde-Wright and P. Y. Bertin, *Workshop on Physics and Instrumentation with 6-12* GeV *Beams*, TJNAF, June 1998; http://www.jlab.org/user_resources/usergroup/proceedings/papers /hyde_wright.pdf
4) X. Ji, Phys. Rev. Lett **78** (1997) 5511; Phys. Rev. D **55** (1997) 7114;
5) A. V. Radyushkin, Phys. Lett.B **380** (1996) 417; **385** (1996) 333;
6) P. A. M. Guichon and M. Vanderhaeghen, Prog. Part. Nucl. Phys **41** (1998);
7) P. Kroll, M. Schurmann and P. A. M. Guichon, Nucl. Phys. A **598** (1996) 435;
8) M. Diehl et al., Phys. Lett. B **411** (1997) 183;
9) M. Guidal and M. Vanderhaeghen, *Workshop on Physics and Instrumentation with 6-12 GeV Beams*, TJNAF, June 1998: hep-ph/9901298; http://www.jlab.org/ user_resources/usergroup/proceedings/papers/guidal.pdf;
10) H. Tang et al., *The NLC Positron Source*, SLAC-PUB-6852;
11) P. Vernin et al., *The ELFE Project: an Electron Laboratory for Europe*, Mainz, 7-9 October 1992; Italian Physical Society conference proceedings **44** (1993), ed. J.Arvieux and E. De Sancti, p. 503;
12) P. Vernin, *New Experimental Techniques and Facilities*, talk at the Conference Nuclear and Particle Physics with CEBAF at Jefferson Lab, Dubrovnik, Croatia, 3 – 10 November 1998;
13) J. M. Finn, *Hall A Workshop on CEBAF at Higher Energies* (1998);
14) G. Alexeev et al., Nucl. Inst. Meth. **A385** (1997) 425;
15) H. Avakian et al., Nucl. Instr. Meth. A **378** (1996) 155;
16) F. Bianchi et al., Nucl. Instr. Meth. A **384** (1996) 67;
17) P. Y. Bertin, computer code BITCH for VCS simulation.

IZAZOV EKSPERIMENATA VIRTUALNOG COMPTONOVOG RASPRŠENJA IZNAD 8 GeV

Raspravljamo teškoće s kojima se sučeljavaju mjerenja reakcija virtualnog Comptonovog raspršenja (VCS) ep$\rightarrow$epγ pri energijama elektrona od 6 do 30 GeV. Posebno se razmatra kinematika duboko virtualnog Comptonovog raspršenja i VCS s velikim prijenosom impulsa. Raspravljamo mjerne uređaje koji su potrebni za takva mjerenja. Za duboko virtualno Comptonovo raspršenje, naglašavamo važnost Bethe-Heitlerovih interferentnih članova koji se mogu mjeriti asimetrijom elektron-pozitron (naboj snopa) i asimetrijom heliciteta elektronskog snopa.